2021 43rd Annual International Conference of the
IEEE Engineering in Medicine & Biology Society (EMBC)
Oct 31 - Nov 4, 2021. Virtual Conference

A Simulation Study for Three Dimensional Tomographic Field Free Line Magnetic Particle Imaging

Damla Alptekin Soydan, Alper Güngör, Can Barış Top

Abstract— **Magnetic Particle Imaging (MPI) is an emerging modality that images the magnetic nanoparticle distribution inside the body. The method is based on the non-linear response of the magnetic nanoparticles to an applied magnetic field. In this study, we present simulation results for three-dimensional (3D) tomographic imaging using an open-bore MPI system that can electronically scan a field free line (FFL). A field of view with $26\times26\times10$ mm^3 volume is imaged with a relatively low gradient field of 0.5 T/m. Imaging results for two 3D phantoms are presented: a letter phantom and a vessel phantom with stenosis regions. Using the system-matrix based reconstruction approach, the images were obtained with the Algebraic reconstruction technique (ART) and alternating direction method of multipliers (ADMM) methods. The stenosis regions were visually recognizable in high SNR conditions with ADMM. The effect of low gradient strength became prominent with increasing noise level, resulting in interlayer coupling artifacts.**

Clinical relevance— **Magnetic Particle Imaging (MPI) is a new tracer-based imaging modality with high-spatiotemporal resolution. MPI can map quantitative distribution of super-paramagnetic iron oxide nanoparticles introduced inside the body. A field free line scanning MPI system with an open configuration can enable imaging of human-size volumes for interventional operations. In this study, we present simulation results for an FFL scanning open MPI system configuration to scan 3D field of view volume electronically. We analyze 3D imaging performance for various SNR levels at a low gradient value of 0.5 T/m that is relevant for clinical-size systems.**

I. INTRODUCTION

Magnetic Particle Imaging (MPI) is a new tracer-based imaging modality that images the spatial distribution of the superparamagnetic iron-oxide nanoparticles (SPIONs) [1]. These particles are usually administered intravenously and used for various applications including vascular imaging, cell tracking and targeting, drug release, and hyperthermia [2]–[5]. MPI method is capable of imaging SPIONs using the non-linear response of the particles to an applied magnetic field. In MPI, a static magnetic field (selection field) with a field free region (FFR) is used to spatially encode the imaging volume. With the effect of the applied selection field, SPIONs are magnetized. Only the SPIONs in the vicinity of the FFR are responsive to an external excitation, thereby localizing the signal in space, while SPIONs out of the FFR are saturated. Applying a dynamic magnetic field (drive field), the FFR is scanned across the field of view (FOV) and the SPION response is picked up inductively. Since the instantaneous FFR location is known, an image can be reconstructed by mapping the signal received from the SPIONs.

Damla Alptekin Soydan, Alper Güngör, and Can Barış Top are with the Aselsan Research Center, ASELSAN AŞ., Ankara, Turkey
Corresponding author: dasoydan@aselsan.com.tr

Depending on the coil configuration, the FFR can be a field free point (FFP) or a field free line (FFL). Compared to FFP configuration, FFL provides improved signal-to-noise ratio (SNR) due to high number of responsive SPIONs inside the larger volume of the FFR. In three-dimensional (3D) imaging, the entire FOV can be sampled by rotating and translating the FFL. This task can be achieved mechanically or electronically; however, the latter may be preferable for clinical applications since it removes the need for mechanical positioning of the imaging system [6], [7]. For FFL scanning MPI, closed bore and single sided imaging systems have been proposed [8], [9]. Despite having the advantage of high coil efficiency, closed bore scanning systems may hinder the use of MPI for interventional applications. On the other hand, single-sided configurations have limited penetration depth. Recently, our group have proposed an open-bore MPI system that is free of field degradation with depth and capable of electronically scanning of an FFL [10]. By controlling the coil currents, the FFL can be electronically rotated, and translated in three dimensions. The performance of the imaging system was analyzed in two-dimensional (2D) simulations for different type of numerical phantoms, reconstruction methods, and trajectories [11]. In addition to the simulation studies, a prototype system was developed and the experiments were conducted [12]. Experiment results showed that for a gradient field of 0.6 T/m, 2D phantoms with resolution down to 2.5 mm can be imaged.

In MPI systems, the resolution of the reconstructed image relies on the particle properties, selection field gradient, drive field properties, and the signal-to-noise ratio (SNR) of the received signal [13]. To generate a high gradient strength, high currents needs to be applied to the field generating coils. This brings additional technical difficulties, such as sophisticated and expensive hardware requirements, and high cooling system demands. Due to these technical challenges, gradient of the clinical-size systems are limited [14].

In this study, we used a 0.5 T/m gradient FFL scanning MPI system with an open scanner configuration to image 3D numerical phantoms. The MPI system is modelled according to the specifications of the developed prototype system [12]. Using the system-matrix based approach, the linear system of equations is solved with algebraic reconstruction technique (ART) and alternating direction method of multipliers (ADMM). We compare the results in terms of image quality for various SNR values.

978-1-7281-1178-0/21/$31.00 ©2021 IEEE

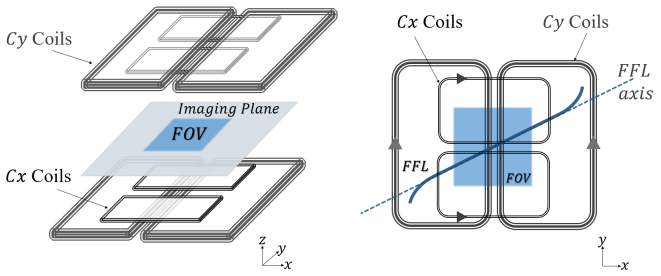

Fig. 1: Open configuration for the electronically rotating and translating FFL. Using two orthogonal coil groups, Cx and Cy, FFL can be generated at any arbitrary direction.

II. METHODS

A. FFL Rotation and Translation

The selection field with field free line is generated using a bi-planar gradient coil configuration as shown in Fig. 1. Coils that generate FFL in the x-axis and y-axis are donated as Cx coils and Cy coils, respectively. For both coil groups, the magnetic field (selection) is in the z-direction, whereas the magnetic field gradient is orthogonal to the magnetic field direction. FFL is rotated by adjusting the currents of the Cx and Cy coils for a desired rotation angle θ. The selection field currents applied to coils are:

$$I_x = I_{x_0}\, cos(\theta)\,, \qquad I_y = I_{y_0}\, sin(\theta) \tag{1}$$

where I_{x_0} and I_{y_0} are the excitation amplitudes of the Cx and Cy coil groups that generates desired gradient in the x- and y- directions, respectively. In order to translate the FFL in the vertical (z-) direction, the currents are applied to upper and lower coil groups as follows:

$$\begin{aligned} I_{i,upper} &= c_i(z)\; I_i(1+\alpha_i(z)) \\ I_{i,lower} &= c_i(z)\; I_i(1-\alpha_i(z)) \end{aligned} \tag{2}$$

In (2), i indicates the type of coil group (Cx or Cy), $\alpha_i(z)$ is a coefficient, which is an odd function of z. $c_i(z)$ is a compensation factor to maintain a constant gradient for any z-position of the imaging plane. After shifting the rotated FFL to the desired imaging plane, the FFL is scanned in the horizontal direction by adding a homogeneous time varying magnetic field (drive field) in the z-direction.

B. Scanning Configuration

For the numerical simulations, the coil parameters (shape, size, number of turns), FOV size, and magnetic field parameters (selection field gradient, drive field amplitude and frequency) were selected according to specifications of the prototype system [12]. An FFL with 0.5 T/m selection field gradient was modeled. An imaging FOV of 26×26×10 mm^3 was discretized with 2×2×2 mm^3 cells. Imaging plane was shifted to the desired position by asymmetrical feeding of the upper and lower coils. At each imaging plane position, FFL was rotated with 3 degree steps. For each rotation angle, FFL was horizontally scanned with a 13 mT amplitude 25 kHz drive field. The received signal at each rotation angle was modeled using the MPI signal equation

$$\begin{aligned} u\,(t) &= -\frac{\partial}{\partial t}\mu_0 m \int_V c\,(\boldsymbol{r})\,\mathcal{L}\,(\beta\,|\mathbf{H}\,(\boldsymbol{r},t)|)\,\frac{\mathbf{H}\,(\boldsymbol{r},t)}{|\mathbf{H}\,(\boldsymbol{r},t)|}\cdot\mathbf{p}(\boldsymbol{r})\,dr \\ m &= M_{sat}\,V, \qquad \beta = \frac{M_{sat}\,V\,\mu_0}{k_B\,T} \end{aligned} \tag{3}$$

where $\boldsymbol{r}$ is the position vector, $\boldsymbol{r} = (x, y, z)$, μ_0 is free space magnetic permeability, $c(\boldsymbol{r})$ is the magnetic particle distribution, $\mathcal{L}(\cdot)$ is the Langevin function. $\mathbf{H}(\boldsymbol{r}, t)$ is the total magnetic field, $\mathbf{p}(\boldsymbol{r})$ is the receive coil sensitivity, M_{sat} is the saturation magnetization (0.6/μ_0), $V(m^3)$ is the volume of the particle, k_B is the Boltzmann constant (1.38×10^{-23}), T is particle temperature (305 °K). The receiver sensitivity was assumed to be homogeneous inside the FOV. The particle diameter was taken as 25 nm. A 50 cycle drive field was applied at each FFL angle, and the received signal was sampled with 5 MS/s sampling rate. The system matrix was obtained in time domain by sweeping a single-voxel phantom across the FOV and calculating the received signal for each FFL.

C. Image Reconstruction

For image reconstruction, the time domain system matrix was transformed to the frequency domain using FFT. Frequency components up to 20 harmonics were used for reconstruction, excluding the first harmonic. The received signal for the numerical phantoms was calculated using in-house developed MPI simulator. The noise was modeled as additive white Gaussian noise and added to the received signal to simulate 10 dB, 20 dB, and 30 dB SNR levels. A linear system of equations that relates the system matrix, image, and the received signal can be expressed as

$$\mathbf{A}\,\mathbf{x} + \mathbf{n} = \mathbf{b}, \tag{4}$$

where $\mathbf{A} \in \mathbb{C}^{M\times N}$ is the filtered system matrix, $\mathbf{x} \in \mathbb{R}^N$ is the unknown particle concentration, $\mathbf{b} \in \mathbb{C}^M$ is the data vector, and $\mathbf{n} \in \mathbb{C}^M$ is the noise. Here N is the total number of voxels, and M is the total number of frequency-angle samples obtained after filtering.

Two numerical phantoms having five layers in the z-direction were used for the performance analyses (Fig. 2). Each layer has 2 mm thickness. The first phantom is a numerical vessel phantom including stenosis regions in each layer. Stenosis regions are indicated with an arrow and the size of the stenosis regions are given in Table 1. The second phantom is made of three letters representing the particle distribution. Two particle free layers are placed in between letters to observe the effects of interlayer coupling in reconstructed images.

For image reconstruction, two different algorithms; namely ART and ADMM, were used to find the solution of an optimization problem involving different regularization terms. The ART reconstruction is used to solve the regularized least squares problem [13]:

$$\arg\min_{\mathbf{x}} \|\mathbf{A}\mathbf{x} - \mathbf{b}\|^2 + \lambda\|\mathbf{x}\|^2, \tag{5}$$

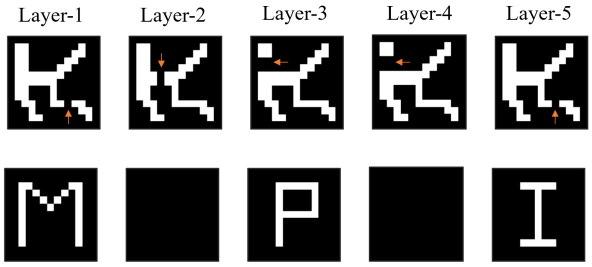

Fig. 2: Numerical phantoms used in the study. (Top) Vessel phantom with stenosis regions. (Bottom) Letter phantom with 2 particle free layers.

TABLE I: Size of Stenosis Regions for Vessel Phantom

Layers	**1**	**2**	**3**	**4**	**5**
Stenosis Size (mm^2)	2×2	2×4	4×4	4×4	2×2

where λ is the regularization parameter. For each iteration (i), the difference between two successive images was calculated using $\|\mathbf{x}^{(i)} - \mathbf{x}^{(i-1)}\|/\|\mathbf{x}^{(i-1)}\|$ and the solver was stopped after reaching a convergence threshold of 10^{-4}.

For ADMM reconstruction, a constrained optimization problem that minimizes a linear combination of the l_1-norm and total variation (TV) of the image is formulated as:

$$\begin{aligned} &\arg\min_{\mathbf{x}} \ \alpha \left\|\mathbf{x}\right\|_1 + (1-\alpha)\, TV\left(\mathbf{x}\right) \\ &s.t \quad \left\|\mathbf{A}\mathbf{x} - \mathbf{b}\right\|_2 < \epsilon, \end{aligned} \tag{6}$$

where $TV(\cdot)$ is total variation function, α is a weighting factor between l_1-norm and TV, and ϵ is the bound on the l_2-norm of noise. The parameters α and ϵ were selected by trial and error to get the best image quality. Details of the algorithm can be found in [15].

III. RESULTS AND DISCUSSION

To observe the vertical translation of the FFL, normalized sensitivity map is computed using the sytem matrix (Fig. 3). The top row in Fig. 3 shows sensitivity inside the FOV when the FFL is at first layer. As expected, the first layer is more sensitive than the other layers. However, there is a close resemblance between the sensitivity of the adjacent layers due to the low gradient strength. As the FFL moves along slices, the sensitive region changes depending on the layer that FFL resides.

The ART and ADMM reconstruction result of the vessel phantom is given in Fig. 4. The reconstructed images are compared quantitatively using the structural similarity index measure (SSIM) and normalized root mean square error (nRMSE) metrics. The SSIM metric was calculated using the built-in *ssim* function of MATLAB, and nRMSE is defined as:

$$\text{nRMSE} = \frac{\|\mathbf{x} - \mathbf{x}_{ref}\|_2}{\|\mathbf{x}_{ref}\|_2}, \tag{7}$$

where $\mathbf{x}_{ref}$ is the reference image vector.

Similar to the results given in [16], ADMM method resulted in better imaging performance compared to ART,

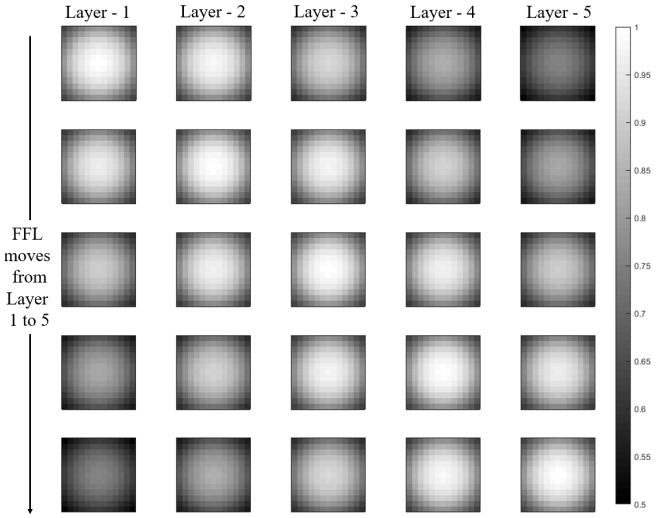

Fig. 3: Normalized 2D sensitivity maps inside FOV for different layers. Rows show the 2D sensitivity at each z layer. At the top row, FFL is at Layer -1. As FFL moves along from top layer to bottom layer, sensitive regions change accordingly.

especially at lower SNR values. ADMM method is able to identify the stenosis regions in all layers except the second layer. The second layer was affected from the particle distribution in adjacent layers due to relatively low gradient of 0.5 T/m. Therefore, 2×4 mm^2 stenosis region appeared in both first and third layers. Even though the first and last layers have a smaller stenosis size (2×2 mm^2) than the second layer, stenoses in these layers can be identified clearly as these layers have only one neighboring layer. The results suggest that stenosis regions can be identified with ADMM method for 30 dB and 20 dB SNR values; however, for 10 dB SNR the gradient is not sufficient for an artifact-free reconstruction.

The ADMM reconstruction result of letter phantom is given in Fig. 5. The three letters in different imaging planes can be identified by visual inspection. However, particle distribution is observed in particle free layers due to the similar sensitivity between the layers. This effect become more pronounced for the lower SNR values.

IV. CONCLUSION

In this study, we have presented the 3D simulation results for an open magnetic particle imaging system that can scan a field free line slice-by-slice electronically. Two different reconstruction algorithms, algebraic reconstruction technique (ART) and alternating direction method of multipliers (ADMM) method, were used to obtain images with a relatively low gradient of 0.5 T/m. ADMM showed better imaging performance, and was also more robust to the degrading effect of the noise. In the high SNR scenario, ADMM method was able to identify both letter phantoms and stenosis regions of different sizes. Therefore, the simulation results suggest that it is possible to generate MPI images down to 2 mm resolution with a relatively low gradient level of 0.5 T/m, which is relevant for a clinical scanner. Future studies will

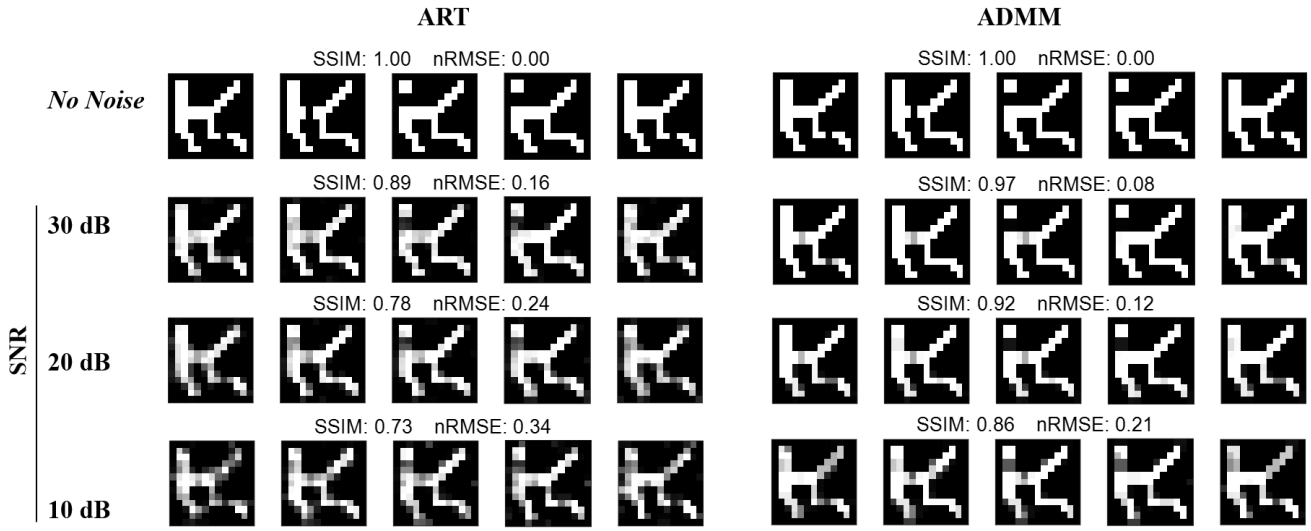

Fig. 4: Reconstructed images of the vessel phantom using ART and ADMM methods for different SNR values. SSIM and nRMSE values for each reconstruction are indicated.

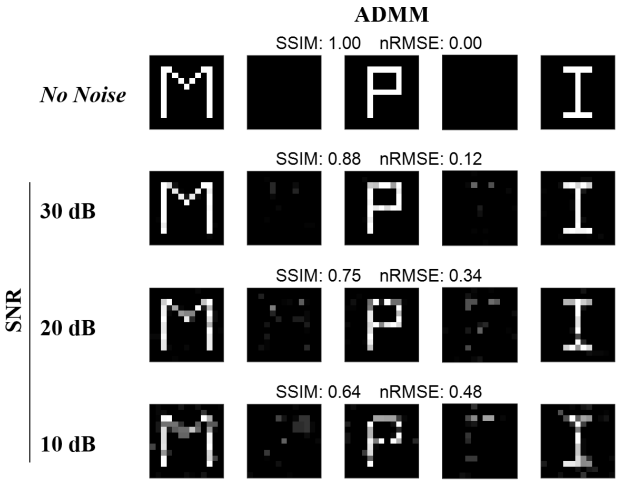

Fig. 5: Reconstructed images of the letter phantom using ADMM method

involve experiments and efficient trajectories for 3D imaging to optimize both imaging time and image quality.

REFERENCES

[1] B. Gleich and J. Weizenecker, "Tomographic imaging using the nonlinear response of magnetic particles," *Nature*, vol. 435, no. 7046, pp. 1214–1217, Jun. 2005.

[2] N. Talebloo, M. Gudi, N. Robertson, and P. Wang, "Magnetic Particle Imaging: Current Applications in Biomedical Research," *Journal of Magnetic Resonance Imaging*, vol. 51, no. 6, pp. 1659–1668, 2020.

[3] Z. W. Tay, P. Chandrasekharan, A. Chiu-Lam, D. W. Hensley, R. Dhavalikar, X. Y. Zhou, E. Y. Yu, P. W. Goodwill, B. Zheng, C. Rinaldi, and S. M. Conolly, "Magnetic Particle Imaging-Guided Heating *in Vivo* Using Gradient Fields for Arbitrary Localization of Magnetic Hyperthermia Therapy," *ACS Nano*, vol. 12, no. 4, pp. 3699–3713, Apr. 2018.

[4] X. Zhu, J. Li, P. Peng, N. Hosseini Nassab, and B. R. Smith, "Quantitative Drug Release Monitoring in Tumors of Living Subjects by Magnetic Particle Imaging Nanocomposite," *Nano Letters*, vol. 19, no. 10, pp. 6725–6733, Oct. 2019.

[5] B. Zheng, M. P. von See, E. Yu, B. Gunel, K. Lu, T. Vazin, D. V. Schaffer, P. W. Goodwill, and S. M. Conolly, "Quantitative Magnetic Particle Imaging Monitors the Transplantation, Biodistribution, and Clearance of Stem Cells In Vivo," *Theranostics*, vol. 6, no. 3, pp. 291–301, Jan. 2016.

[6] M. Weber, K. Bente, A. v. Gladiß, and T. M. Buzug, "MPI with a mechanically rotated FFL," in *2015 5th International Workshop on Magnetic Particle Imaging (IWMPI)*, Mar. 2015.

[7] T. Knopp, M. Erbe, S. Biederer, T. F. Sattel, and T. M. Buzug, "Efficient generation of a magnetic field-free line: Efficient generation of a magnetic field-free line," *Medical Physics*, vol. 37, pp. 3538–3540, Jun. 2010.

[8] K. Bente, M. Weber, M. Graeser, T. F. Sattel, M. Erbe, and T. M. Buzug, "Electronic field free line rotation and relaxation deconvolution in magnetic particle imaging," *IEEE Trans. Med. Imag.*, vol. 34, no. 2, pp. 644–651, 2015.

[9] A. Tonyushkin, "Single-sided field-free line generator magnet for multi-dimensional magnetic particle imaging," *IEEE Transactions on Magnetics*, vol. 53, no. 9, pp. 1–6, 2017.

[10] C. B. Top, S. Ilbey, and H. E. Güven, "Electronically rotated and translated field-free line generation for open bore magnetic particle imaging," *Medical Physics*, vol. 44, no. 12, pp. 6225–6238, 2017.

[11] C. B. Top, A. Güngör, S. Ilbey, and H. E. Güven, "Trajectory analysis for field free line magnetic particle imaging," *Medical Physics*, vol. 46, no. 4, pp. 1592–1607, 2019.

[12] C. B. Top and A. Güngör, "Tomographic Field Free Line Magnetic Particle Imaging With an Open-Sided Scanner Configuration," *IEEE Trans. Med. Imag.*, vol. 39, no. 12, pp. 4164–4173, Dec. 2020.

[13] T. Knopp and T. M. Buzug, *Magnetic Particle Imaging: An Introduction to Imaging Principles and Scanner Instrumentation*. Berlin Heidelberg: Springer-Verlag, 2012.

[14] M. Graeser, F. Thieben, P. Szwargulski, F. Werner, N. Gdaniec, M. Boberg, F. Griese, M. Möddel, P. Ludewig, D. van de Ven, O. M. Weber, O. Woywode, B. Gleich, and T. Knopp, "Human-sized magnetic particle imaging for brain applications," *Nature Communications*, vol. 10, no. 1, p. 1936, Dec. 2019.

[15] S. Ilbey, C. B. Top, A. Güngör, T. Çukur, E. U. Saritas, and H. E. Güven, "Comparison of System-Matrix-Based and Projection-Based Reconstructions for Field Free Line Magnetic Particle Imaging," *International Journal on Magnetic Particle Imaging*, vol. 3, no. 1, Mar. 2017.

[16] S. Ilbey, C. B. Top, T. Çukur, E. U. Saritas, and H. E. Güven, "Image reconstruction for Magnetic Particle Imaging using an Augmented Lagrangian Method," in *2017 IEEE 14th International Symposium on Biomedical Imaging (ISBI 2017)*, Apr. 2017, pp. 64–67.